ACCSCIENCE PUBLISHING

Materials Science in Additive Manufacturing

ORIGINAL RESEARCH ARTICLE

Data-driven prediction and tribological analysis of FDM-printed MXene-reinforced PLA composites

Sundarasetty Harishbabu[1], Santosh Kumar Sahu[1]*, P. S. Rama Sreekanth[1], Ravi Kumar V[2], and Jana Petrů[3]*

[1]School of Mechanical Engineering, VIT-AP University, Amaravati, Andhra Pradesh, India

[2]Department of Mechanical Engineering, Amrita School of Engineering, Amrita Vishwa Vidyapeetham, Bengaluru, Karnataka, India

[3]Department of Machining, Assembly and Engineering Metrology, Faculty of Mechanical Engineering, VSB-Technical University of Ostrava, Ostrava, Czech Republic

***Corresponding authors:**
Santosh Kumar Sahu (santoshkumar.sahu@vitap.ac.in);
Jana Petrů (jana.petru@vsb.cz)

Citation: Harishbabu S, Sahu SK, Sreekanth PSR, Kumar R, Petrů J. Data-driven prediction and tribological analysis of FDM-printed MXene-reinforced PLA composites. *Mater Sci Add Manuf*. doi: 10.36922/MSAM026390099

Received: September 26, 2026

1st revised date: October 21, 2026

2nd revised date: October 28, 2026

Accepted: October 29, 2026

Published online: November 25, 2026

Copyright: © 2026 Author(s). This is an Open-Access article distributed under the terms of the Creative Commons Attribution License, permitting distribution, and reproduction in any medium, provided the original work is properly cited.

Publisher's Note: AccScience Publishing remains neutral with regard to jurisdictional claims in published maps and institutional affiliations.

Abstract

The growing demand for lightweight, wear-resistant polymer composites has driven research into nanofiller-reinforced composites and advanced predictive modeling approaches to improve tribological performance and material reliability. This research focused on enhancing and predicting the tribological properties of polylactic acid (PLA) reinforced with MXene nanofiller using advanced data-driven models. The test samples were fabricated based on a Box–Behnken response surface methodology (RSM) design using fused deposition modeling (FDM) to analyze the effects of reinforcement content (0–0.05 wt.%), sliding speed (200–500 RPM), sliding distance (500–1,500 mm), and applied load (10–30 N) at three levels on specific wear rate (SWR) and coefficient of friction (COF). The SWR varied from 2.2×10^{-4} to 5.7×10^{-3} mm^3/N·mm, while the COF ranged from 0.240 to 0.582, indicating a strong dependence on these factors. Analysis of variance reveals that applied load and interaction effects dominate wear behavior, while sliding speed, sliding distance, and reinforcement significantly influence frictional response. The RSM models demonstrated strong predictive capability with R^2 values of 0.9478 for SWR and 0.7996 for COF. Furthermore, machine learning models were developed, including multiple linear regression, random forest regression, and gradient boosting regression. During experimental validation, the gradient boosting regression model achieved R^2 values of 0.8879 for SWR and 0.7710 for COF. Moreover, SHapley Additive exPlanations analysis showed that feature importance depended on the response and machine-learning model, with applied load, reinforcement content, sliding distance, and sliding speed contributing differently to the model predictions. The findings provide a framework for optimizing FDM-printed MXene/PLA components for wear-resistant applications in lightweight engineering, automotive, and other tribological systems.

Keywords: Polymer composites; MXene; Tribology; Response surface methodology; Machine learning

1. Introduction

Additive manufacturing has become an important technique for producing thermoplastic components with complex shapes, reduced material waste, and high design flexibility.[1,2] Thermoplastics such as polylactic acid (PLA) are widely used because of their lightweight, recyclability, and ease of processing. However, pure thermoplastics often exhibit limited wear resistance and functional performance, which restricts their use in tribological applications. To overcome these limitations, nano-fillers such as carbon nanotubes, graphene, nanoclay, nano-silica, and metal oxide nanoparticles are incorporated into polymer matrices.[3,4] These nanofillers can improve wear resistance.[5] In additive manufacturing, the properties depend on filler dispersion, filler content, printing temperature, layer thickness, and build orientation. Therefore, nanofiller-reinforced thermoplastics are promising materials for lightweight, functional, and high-performance printed parts.[6] Several researchers have focused on PLA reinforced with nanofillers to achieve good tribological properties. Kumar *et al.*[7] investigated PLA reinforced with graphene nanoparticles (GNP) at 0.5–2 wt% in PLA, which significantly enhanced performance in the 1.5 wt% GNP composite, exhibiting a 68.9% increase in hardness and a 67.4% reduction in wear rate compared to neat PLA. Al Abir *et al.*[8] found that PLA composites reinforced with 5 wt.% short carbon fiber and 5 wt.% GNP, resulting in a 30% increase in hardness and a ~220% rise in elastic modulus compared to neat PLA, and also a reduction in the friction coefficient to 0.49–0.60 (vs. 0.71 for PLA), achieved a five times lower wear rate, indicating great improvement in mechanical and tribological performance. Ramachandran *et al.*[9] reported a significant improvement in the mechanical and tribological behavior of PLA/nano-silica composites with various wt.% of 0, 2, 4, 6, and 8, fabricated via fused deposition modeling (FDM) at 8 wt.% of nano-silica, achieving 52 MPa tensile strength, 52 MPa flexural strength, and 52 MPa hardness, along with a reduced coefficient of friction (COF) and specific wear rate (SWR). Vishal *et al.*[10] investigated PLA with 0%, 1%, 3%, 5%, and 7% silicon and tested their mechanical and wear properties. As a result, 5% silicon content had a Shore D hardness of 95, tensile strength of 55 MPa, flexural strength of 60 MPa, impact strength of 5.9 kJ/m^2, and compression strength of 11.8 MPa. The composite also showed low specific wear of 2×10^{-3} mm^3/Nm and a COF of 0.11. The study concluded that 5% silicon reinforcement improves PLA's mechanical strength and wear resistance. Sirin *et al.*[11] evaluated the tribological behavior of graphite-modified Lubri PLA fabricated by additive manufacturing with varying infill patterns. The best performance was observed for Lubri PLA with diagonal three-dimensional (3D) infill, with a COF of 0.245, SWR of 0.050, and vibration value of 0.041 mm/s^2. Batista *et al.*[12] reported the tribological performance of copper- and aluminum-reinforced PLA parts fabricated by additive manufacturing; the results showed that reinforced PLA increased surface roughness by more than 300%, and Al-reinforced PLA improved hardness by over 75%. The study also reported that wear material loss was reduced by about 50%, indicating better durability of reinforced PLA parts. Zawadzki *et al.*[13] investigated FDM-printed PLA and PLA-carbon fiber (CF) composites at extrusion temperatures of 190 °C–240 °C using two-wall and three-wall internal structures. The results showed that 190 °C–220 °C produced stable COF, while PLA-CF reduced friction and improved wear resistance compared with neat PLA. The two-wall structure minimized wear and friction, whereas the three-wall structure gave more consistent COF. Fouly *et al.*[14] developed 3D-printed PLA/corn cob green composites with 0–20 wt.% corn cob filler for artificial hip-joint applications; as a result, at 10 wt.% corn cob, hardness increased by 10%, Young's modulus by 6%, compressive strength by 12%, and wear resistance by 150%; the lowest friction coefficient was 0.33, lower than neat PLA at 0.36. Singh *et al.*[15] optimized FDM process parameters of PLA-nanographite composites using Taguchi Design of Experiments and pin-on-disc wear testing and reported that composition, raster angle, and infill density significantly affected wear performance, with wear-strength values of 0.0080–0.0100 mm^3/min. Hozdić and Hozdić[16] investigated FDM-printed PLA and PLA+CF using linear, triangular, and hexagonal infill patterns at 30%, 60%, and 100% density, followed by seven-day mineral oil exposure. The results showed that PLA reached 31.5 MPa tensile strength, while PLA+CF reached 33.4 MPa tensile strength and 500 MPa Young's modulus at 100% infill. Oil exposure increased PLA elongation by 76% and improved PLA+CF tensile strength by 6.9%, showing better structural stability. Mzali *et al.*[17] evaluated FDM-printed PLA surfaces with raster orientations of [0°/90°], (+15°/−75°), (+30°/−60°), and (+45°/−45°) using a reciprocating tribometer. Under low load, changing the raster orientation from (+45°/−45°) to (0°/90°) reduced the friction coefficient by about 71% and decreased wear track width by about 41%. Lasch *et al.*[18] investigated the tribological properties of FDM-printed PLA, TPU, bronze-filled PLA, and their composite combinations using a pin-on-disc test. Pure bronze-filled PLA showed the lowest wear rate of $K \approx 0.9 \times 10^{-5}$ mm^3/Nm, while pure PLA showed the lowest friction coefficient of $\mu \approx 0.24$ but the highest wear rate of $K \approx 16.7 \times 10^{-4}$ mm^3/Nm. The 75% bronze/25% PLA composite gave the best-balanced performance in terms of wear rate and COF. Keshavamurthy *et al.*[19] developed FDM-printed PLA composites reinforced

with 5 wt% and 10 wt% boron nitride (BN). The results showed that 5 wt% BN and 10 wt% BN improved tensile strength to 74 MPa and 82 MPa, respectively, while surface roughness decreased by 13.01% and 24.61%. The 10 wt% BN composites also showed better wear resistance, with wear reduced to 0.10 µm compared with 0.14 µm for neat PLA at 250 rpm. Abdulla *et al.*[20] studied the dry sliding wear behavior of 3D-printed PLA and predicted wear rate using an ANN model. The SWR ranged from 0.000034229 to 0.000404375 mm^3/Nm, with the lowest wear obtained at 220°C extrusion temperature, 40 mm/s print speed, 335 cm/s sliding velocity, 15 N load, and 80% infill. The ANN model shows that there is good agreement between actual and predicted wear values. Ahmad *et al.*[21] highlighted that optimized PLA printing parameters could achieve a tensile strength of 45.81 MPa, tensile strain of 12.13%, breaking load of 359.34 kgf, and extension of 7.21 mm. Artificial intelligence/machine learning (ML)-based optimization also predicted improved dynamic properties, including a storage modulus of 1619.61 MPa and a loss modulus of 257.38 MPa.

Although previous studies have investigated PLA-based composites, most have focused on experimental characterization for evaluating wear performance, with relatively few studies on optimization techniques such as response surface methodology (RSM) and ML. However, the tribological performance of MXene ($Ti_3C_2T_x$)-reinforced FDM-printed PLA composites remains insufficiently explored, particularly under the combined effects of MXene content and tribological parameters, i.e., sliding speed, sliding distance, and applied load. To address this research gap, the present study integrates Box–Behnken experimental design, experimental tribological testing, comparative machine-learning modeling, and SHapley Additive exPlanations (SHAP)-based model interpretation to investigate and predict the COF and SWR of PLA/MXene nanocomposites. Experimental validation is performed to assess the agreement between predicted and measured responses. SHAP analysis is used to evaluate the relative contributions of input parameters to model predictions, rather than to establish causal relationships or directly demonstrate physical mechanisms. This work applies this integrated approach to the PLA/MXene material system and systematically evaluates its tribological responses.

2. Materials and methods

2.1. Materials

Deltora Biopolymer Pvt. Ltd., Ahmedabad, Gujarat, India, supplied PLA granules with a melt flow index of 2–4 g/10 min, with a specific gravity of 1.30–1.35 g/cm^3. MXene ($Ti_3C_2T_x$) powder with a density of 3.8 g/cm^3 and a purity of > 99% was supplied by Nano Research Element from India. The microstructural study was conducted using transmission electron microscopy. Figure 1A presents the transmission electron microscopy image of MXene, revealing a flake-like laminar morphology with stacked and agglomerated nanosheets. Figure 1B shows the particle size of MXene using ImageJ software (Version 1.54t, National Institutes of Health, USA). It was confirmed that the average particle size is close to 100nm. The flake-like laminar structure provides a high specific surface area, which is beneficial for improving interfacial adhesion and stress transfer in the PLA matrix.[22,23]

2.2. Sample fabrication

The FDM technique was used to fabricate PLA-MXene composite samples for tribological analysis. The fabrication process involves three main stages, namely composition preparation, filament extrusion, and sample printing.

2.2.1. Composite preparation

Figure 2A illustrates the composition preparation process. In this process, the required amounts of PLA and MXene were accurately measured using a digital balance (Shimadzu ATX-224, Shimadzu Co., Kyoto, Japan) for the 0.025 and 0.05 wt% compositions, along with pure PLA. The MXene content was calculated relative to the total mass of the composite. After weighing, MXene was dispersed in ethanol at a 1:30 solid-to-liquid ratio and sonicated for 30 min at 40 kHz to obtain uniform particle dispersion and reduce agglomeration. The PLA granules were added gradually to the MXene solution on a hot plate, and the mixture was continuously stirred at 60 °C until the ethanol evaporated and proper interaction between the PLA matrix and MXene filler was achieved. After achieving a uniform mixture, it was dried in a vacuum oven at 80 °C for 24 h to remove the residual moisture.[24,25]

2.2.2. Filament extrusion and sample printing

Figure 2B presents the process for filament extrusion and sample fabrication. The dried compositions were fed into a filament extruder (AASAVI/25TS/CO/300/30, Aasabi Machinery Pvt. Ltd., India) and were extruded into a continuous filament suitable for FDM printing. Extrusion temperatures ranged from 180 °C to 210 °C, with a screw speed of 30 mm/min, to obtain a uniform filament diameter of 1.75 ± 0.05 mm. The extruded filaments were cooled, collected, and checked for diameter consistency using a micrometer before printing. Finally, the PLA-MXene composite filaments were used to fabricate test specimens using a FlashForge 3D printer (Dreamer, Zhejiang Flashforge 3D Technology Co., Ltd., China)

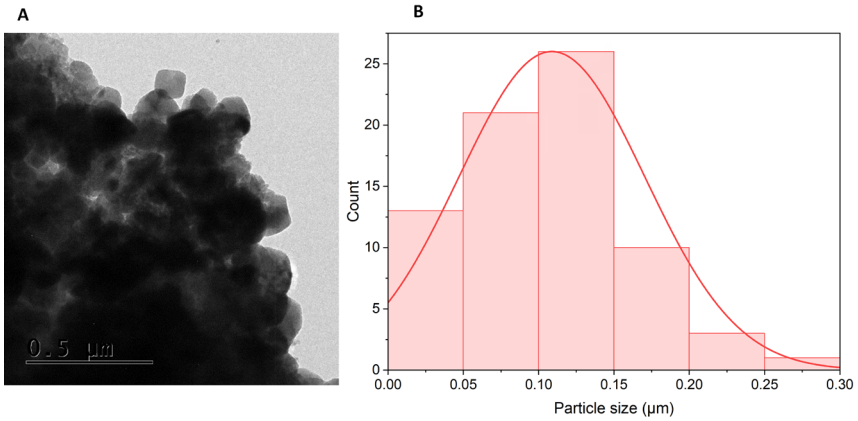

Figure 1. As-received MXene powder. (A) Transmission electron microscopy (TEM) morphology. Scale bar: 0.5 μm; magnification: 100×. (B) Particle-size distribution.

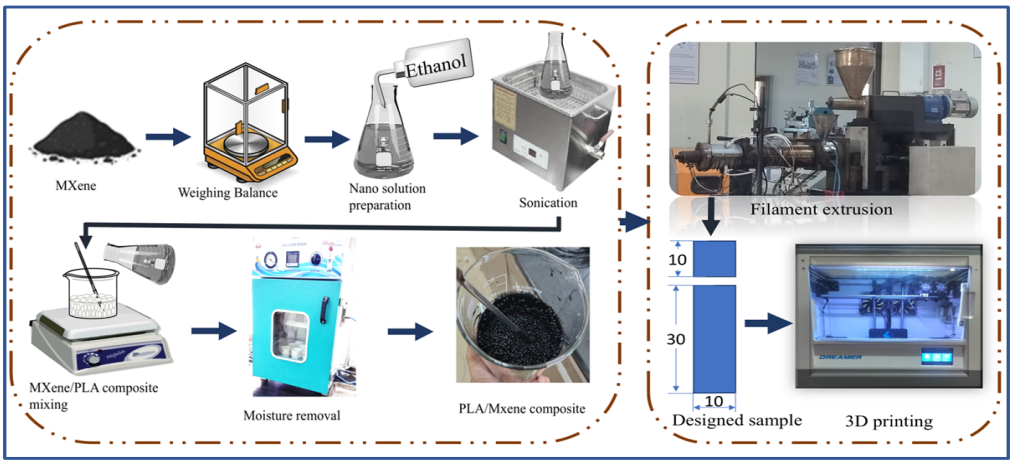

Figure 2. Sample fabrication steps. (A) Composition preparation. (B) Filament extrusion and sample printing.
Abbreviations: 3D: Three-dimensional; PLA: Polylactic acid.

under controlled printing conditions, including a nozzle temperature of 210 °C, a bed temperature of 50 °C, a layer height of 0.2 mm, 100% infill density, and a printing speed of 30mm/s, with a linear raster angle set using FlashForge slicing software (FlashForge 5, Zhejiang Flashforge 3D Technology Co., Ltd., China). The samples were printed in accordance with the required American Society for Testing and Materials standard. After printing, the specimens were removed from the build plate, visually inspected for defects such as warping, poor bonding, or incomplete layers, and then conditioned at room temperature before further characterization.[26]

2.3. Statistical analysis

2.3.1. Experimental design

The experiments were designed using the Design of Experiments based on RSM. A Box–Behnken Design with 31 randomized runs was generated to evaluate the effect of factors on the response, as shown in Tables 1 and 2. The factors were studied at three levels, as shown in Table 1.[27] The design included 24 non-center design points and seven replicated center points, a total of 31 experimental runs. The experimental factors were transformed into coded values of −1, 0, and +1, corresponding to their low, medium, and high levels, respectively. The regression equations were developed using these coded factor values in Design-Expert.[28,29]

2.3.2. Analysis of variance

To evaluate the significance of the fitted model, analysis of variance was performed at a 95% confidence level. The *F*-test and corresponding p-values were computed for each factor to assess the statistical significance of the model. The terms are considered statistically significant when the *p*-value is less than 0.05, indicating a meaningful effect on

Table 1. Levels and factors for experimental design

Factors	Units	Low Level (−1)	Medium level (0)	High level (+1)
Reinforcement (W)	wt. %	0.00	0.025	0.05
Speed (S)	RPM	200	350	500
Sliding distance (D)	mm	500	1000	1500
Applied load (L)	N	10	20	30

Table 2. Experimental design with responses

S. No	Reinforcement (wt.%)	Sliding speed (RPM)	Sliding distance (mm)	Applied Load (N)	Specific wear rate (mm^3/N-mm)	Coefficient of friction
R1	0.025	350	1,000	20	0.0013	0.419
R2	0.025	200	1,000	10	0.0011	0.341
R3	0.025	350	500	30	0.0023	0.570
R4	0.025	500	1,000	10	0.0016	0.426
R5	0.025	200	500	20	0.0014	0.355
R6	0.050	200	1,000	20	0.0007	0.240
R7	0.025	350	1,000	20	0.0008	0.508
R8	0.025	350	1,000	20	0.0006	0.408
R9	0.050	350	1,000	10	0.0057	0.394
R10	0.000	350	500	20	0.0006	0.539
R11	0.025	350	1,500	30	0.0010	0.310
R12	0.000	500	1,000	20	0.0011	0.475
R13	0.050	350	1,000	30	0.0005	0.429
R14	0.000	350	1,000	10	0.0027	0.496
R15	0.000	200	1,000	20	0.0008	0.489
R16	0.000	350	1,000	30	0.0035	0.545
R17	0.025	500	500	20	0.0008	0.383
R18	0.050	350	500	20	0.0002	0.482
R19	0.025	350	1,000	20	0.0009	0.480
R20	0.025	350	500	10	0.0005	0.483
R21	0.000	350	1,500	20	0.0011	0.357
R22	0.025	350	1,500	10	0.0005	0.427
R23	0.050	500	1,000	20	0.0008	0.465
R24	0.025	350	1,000	20	0.0005	0.365
R25	0.025	200	1,000	30	0.0037	0.366
R26	0.025	350	1,000	20	0.0009	0.582
R27	0.050	350	1,500	20	0.0006	0.395
R28	0.025	200	1,500	20	0.0006	0.336
R29	0.025	500	1,000	30	0.0009	0.439
R30	0.025	350	1,000	20	0.0007	0.431
R31	0.025	500	1,500	20	0.0044	0.477

the responses at the 95% confidence level. The accuracy of the model was further assessed using R^2, adjusted R^2, predicted R^2, and the lack-of-fit test.[30,31] The response-surface plots were interpreted in conjunction with the corresponding regression coefficients and analysis of variance (ANOVA) results to ensure that the described trends were consistent with the fitted models and the statistical evidence.

2.4. Experimental analysis

The tribological performance of PLA/MXene composites was evaluated using a pin-on-disk tester (TR-20LE-PHM400-CHM400, DUCOM Instruments Pvt. Ltd., India) under dry-sliding conditions at approximately 24 °C, in accordance with American Society for Testing and Materials G99-23. A dry sliding test was conducted at an ambient temperature of approximately 24 °C using a steel counterface with a hardness of 838 ± 21 HV and a track diameter of 80 mm. The experimental design varied the applied load, sliding speed, sliding distance, and MXene reinforcement content. The SWR and COF were selected as the response variables to evaluate the tribological performance of the composites. The COF was calculated from the stable steady-state region of the friction curve over the complete test duration. The SWR and COF were determined from the experimental measurements using **Equations 1–3**.[32,33] The resulting data were used for RSM analysis and machine learning prediction.

$$\mathrm{SWR} = \frac{\mathrm{V}}{F_N \times \mathrm{L}} \tag{1}$$

$$\mathrm{V} = \mathrm{d} \times \mathrm{A}_p \tag{2}$$

$$\mathrm{COF} = \frac{\mathrm{F}_T}{F_N} \tag{3}$$

where V is the estimated wear volume (mm^3), F_N is the applied normal force (N), L is the sliding distance (mm), d is the wear depth of the rectangular pin (mm), A_p is the cross-sectional area of the pin's worn face (mm^2), and F_T is the tangential friction force (N).

2.5. Machine learning

Machine learning was used to model and predict the relationship between testing parameters and responses, namely SWR and COF. The input parameters included reinforcement content, sliding speed, sliding distance, and applied load. Three regression models, multiple linear regression (MLR), random forest regression (RFR), and gradient boosting regression (GBR), were implemented using Python (3.0, Python Software Foundation, Netherlands) with Scikit-learn. Second-order polynomial features were generated and then standardized using StandardScaler. The hyperparameters of RFR and GBR were optimized using GridSearchCV with five-fold shuffled cross-validation and a random state of 42. Model development and validation were conducted in two stages. Firstly, the 31 experimental runs from the experimental design were used to train the ML models, and their performance was evaluated using the corresponding prediction and performance metrics, including the coefficient of determination (R^2), mean squared error (MSE), root mean squared error (RMSE), and mean absolute error (MAE), as defined in **Equations 4–7**. Secondly, five additional experimental validation samples, independent of the original 31 runs, were used to compare the model-predicted SWR and COF with the experimentally measured responses and independently assess predictive performance. SHAP analysis was subsequently employed to interpret feature contributions to the model predictions and examine model behavior.[34,35]

$$R^2 = 1 - \frac{\sum_{k=1}^{n}(T_k - \breve{T}_k)^2}{\sum_{k=1}^{n}(T_k - \bar{T})^2} \tag{4}$$

$$MAE = \frac{1}{n}\sum_{k=1}^{n}\left|T_k - \breve{T}_k\right| \tag{5}$$

$$MSE = \frac{1}{n}\sum_{k=1}^{n}(T_k - \breve{T}_k)^2 \tag{6}$$

$$RMSE = \sqrt{MSE} \tag{7}$$

where n, $T_{k,}$ $\bar{T}$, and $\breve{T}_k$ are the number of experimental runs, the values obtained from experimental runs, the mean of all experimental values, and the predicted value associated with the observation, respectively.

2.5.1. Multiple linear regression

A baseline statistical learning model to analyze the linear relationship between factors and responses is MLR. The model parameters were established using the least squares method. Multicollinearity was assessed to ensure stable coefficient estimates. MLR provides a simple and interpretable baseline for comparison with advanced machine learning models. The model assumes a linear combination of predictors and is expressed as **Equation 8**:[36]

$$T = \delta_0 + \delta_1 W + \delta_2 S + \delta_3 D + \delta_4 L + \in \tag{8}$$

where T represents the tribological properties; δ_0 is the intercept; δ_1, δ_2, δ_3, and δ_4 are the regression coefficients; W, S, D, and L are the input factors; and $\in$ is the error term.

2.5.2. Random forest regression

Random forest regression is an ensemble learning

technique that constructs multiple decision trees using bootstrap sampling of the dataset and randomly selected feature subsets. The prediction is obtained by averaging the outputs of all the individual trees, which tends to improve model stability and avoid overfitting. This method is particularly effective in capturing complex nonlinear relationships between input variables and responses, as shown in **Equation 9**:[37]

$$T = \frac{1}{N}\sum_{k=1}^{N} f_i(x) \quad (9)$$

Where $fi(x)$ represents the prediction of the ith decision tree and N is the total number of trees in the forest.

2.5.3. Gradient boosting regression

Gradient boosting regression is an advanced ensemble learning method that builds predictive models sequentially, where each new model is trained to correct the errors of the previous models. This iterative optimization process minimizes a defined loss function using gradient descent, leading to high prediction accuracy. The final model is formed by combining weak learners (decision trees) weighted according to their contribution to reducing error. The prediction is expressed in **Equations 10** and **11**:[38]

$$F(x) = \sum_{g=1}^{G} \varphi_g h_g(x) \quad (10)$$

$$F_g(x) = F_{g-1}(x) - \eta \frac{\partial L(y, F(x))}{\partial F(x)} \quad (11)$$

where $h_g(x)$ represents the weak learner (decision tree), φ_g is the learning rate weight, and G is the total number of boosting stages. The model minimizes a loss function $L(y, F(x))$ using gradient descent optimization.

2.6. Experimental validation

To assess the predictive accuracy of machine learning models, an experimental validation was conducted using five new conditions that are not included in the dataset used for model training, as shown in Table 3.

3. Results and discussion

3.1. Experimental analysis

Table 2 presents the experimental design and corresponding responses. Figure 3A–3B illustrates the experimentally measured SWR and COF, respectively, for the 31 experimental runs (R1–R31). SWR ranged from 0.0002 to 0.0057, with the minimum values observed in R13, R20, and R22 and the maximum value in R9. COF ranged from 0.2403 to 0.582, with the minimum value observed in R6 and the maximum value in R26. Notably, R6 exhibited a relatively low SWR of 0.0007 alongside the minimum COF of 0.2403. However, R16 exhibits an SWR of 0.0035 and a COF of 0.545, whereas R31 exhibits an SWR of 0.0044 and a COF of 0.477. These experimental observations illustrate the variation in both responses across the tested conditions. Although the responses do not exhibit a consistent proportional correspondence in these selected examples, this observation alone does not establish statistical independence or determine the strength of their association. Accordingly, the effects of the experimental parameters on SWR and COF are evaluated separately using RSM and machine learning models.

Optical microscopy images of the wear tracks of pure PLA and 0.05 wt.% MXene-reinforced PLA are presented in Figure 4A–4F after sliding at a speed of 500 rpm and a sliding distance of 1,500 mm. Figure 4A–4C shows the wear tracks of pure PLA at applied loads of 10, 20, and 30 N, respectively. At 10 N, pure PLA exhibits minor plowing with limited surface deformation. At 20 N for pure PLA, the wear track shows more distinct grooves and plowing marks, indicating increased surface deformation with increasing load. At 30 N for pure PLA, pronounced wear grooves and plowing marks are observed, reflecting greater deformation of the worn surface.[39] Figure 4D–4F shows the wear tracks of the 0.05 wt.% PLA/MXene composite at 10, 20, and 30 N, respectively. At 10 N for the 0.05 wt.% PLA/MXene composite, several small pits are visible on the worn surface, indicating localized material removal during sliding. At 20 N for the 0.05 wt.% PLA/MXene composite,

Table 3. Dataset for experimental validation

S. No.	Reinforcement wt.%	Applied load (N)	Sliding distance (mm)	Sliding speed (RPM)
1	0.050	25	1,451	420
2	0.000	30	656	247
3	0.050	20	1,366	380
4	0.050	30	1,470	450
5	0.025	15	682	255

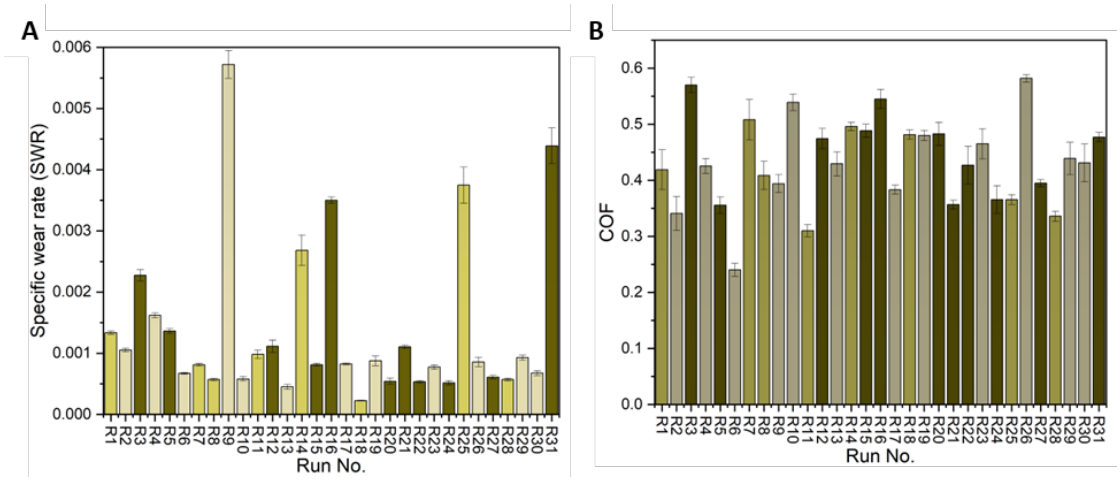

Figure 3. Experimental results for (A) specific wear rate and (B) coefficient of friction (COF)

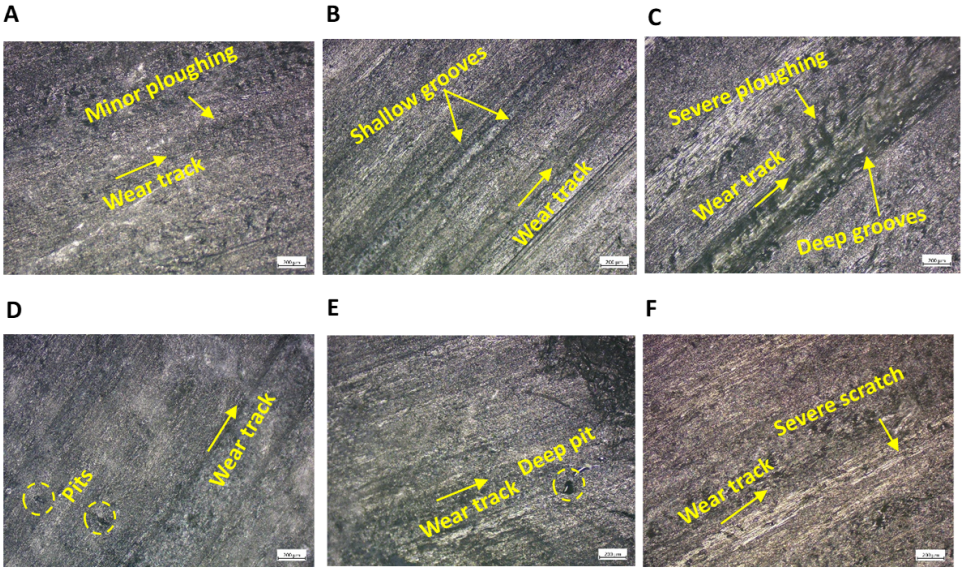

Figure 4. Optical micrographs of wear tracks for (A–C) pure PLA and (D–F) PLA/MXene composite containing 0.05 wt.% MXene at applied loads of 10, 20, and 30 N, respectively, at a sliding speed of 500 RPM and a sliding distance of 1,500 mm. Scale bar: 200 μm; magnification: 200×.

the surface is characterized by a prominent single deep pit, suggesting localized and concentrated surface damage. At 30 N for the 0.05 wt.% PLA/MXene composite, deep and distinct scratches are observed along the sliding direction, accompanied by more pronounced surface deformation.[40] The observed wear-track features suggest that adding MXene altered the surface damage behavior of PLA under the applied loads.

3.2. Analysis of variance

3.2.1. Specific wear rate

Table 4 presents the results of the SWR ANOVA. A *p*-value of less than 0.0001 indicates that the model is statistically significant and suitable for SWR prediction. Among the linear factors, the applied load stands alone as a significant factor with a *p*-value of 0.0023. Compared to the factors alone, the integration effects have a more significant influence on SWR. The interaction between reinforcement and applied load (W × L), having a p-value less than 0.0001, indicates a highly significant result, followed by sliding speed vs. sliding distance (S × D), and sliding speed vs. applied load (S × L) with *p*-values less than 0.0001 and 0.0007, respectively. Similarly, for quadratic terms such as W^2 and S^2 with p-values less than 0.0001 and 0.0002, and the higher-order terms, such as $W^2 \times L$, $S^2 \times D$, $S \times D^2$, $W^2 \times S^2$, and $W^2 \times D^2$with p-values less than 0.0001, 0.0090, 0.0007, less than 0.0001, and less than 0.0001, respectively. This confirms that the SWR response follows a complex nonlinear trend. Meanwhile, a lack-of-fit test

with a *p*-value of 0.0964 shows a statistically insignificant result, indicating that the model is accurately fit for the experimental data. The model also shows good prediction capability, as indicated by the coefficient of determination R^2 value of 94.78%; an adjusted R^2 of 90.21% confirms good model reliability after considering the number of terms, while the predicted R^2 value of 0.7969 indicates acceptable prediction. ANOVA reveals that the developed model is suitable for predicting SWR. The fitted regression equation for prediction is presented in **Equation 12**. Applied load is the most significant factor, while the interaction terms W × L, S × D, and S × L have major effects on the wear response. The significant quadratic and higher-order terms further demonstrate that the wear behavior is nonlinear and depends on the combined influence of the process parameters.

$$\begin{aligned} SWR = {} & 0.0009 - 0.0001W - 0.0002S - 0.0000D \\ & + 0.0005L - 0.0015WL + 0.0011SD \\ & - 0.0008SL + 0.0022W^2 + 0.0009S^2 \\ & - 0.0016W^2L + 0.0007S^2D + 0.0011SD^2 \\ & - 0.0032W^2S^2 - 0.0025W^2D^2 \end{aligned} \quad (12)$$

Figure 5A–5B illustrates and validates the accuracy and suitability of the predicted model for the SWR. Figure 5A presents a comparison between the actual and predicted values, showing that most data points lie very close to the diagonal reference line, which represents the ideal condition where predicted and actual values are equal. This close clustering indicates that the model predictions strongly agree with the experimental results over the full SWR range of approximately 2.2493×10^{-4} to 5.72069×10^{-3} mm³/N-mm. Only minor deviations are observed, especially at some intermediate and higher SWR values, but these deviations are small and do not indicate serious prediction error. Similarly, Figure 5B shows the normal probability plot of residuals, where the residual points mostly follow the straight reference line, confirming that the prediction errors are approximately normally distributed. The residuals are spread within about -6.0×10^{-4} to $+8.0 \times 10^{-4}$, with most values concentrated near the center, suggesting low random error and no strong systematic error. Therefore, both comparative plots confirm that the regression model provides a reliable prediction of SWR and adequately represents the experimental wear behavior.

Table 4. Analysis of variance for specific wear rate (SWR)

Source	SS	df	MS	*F*-value	*p*-value
Model	0.0000	14	3.449×10^{-06}	20.74	< 0.0001
Reinforcement (W)	1.503×10^{-07}	1	1.503×10^{-07}	0.9039	0.3559
Speed (S)	4.288×10^{-07}	1	4.288×10^{-07}	2.58	0.1278
Sliding distance (D)	1.942×10^{-08}	1	1.942×10^{-08}	0.1168	0.7369
Applied load (L)	2.185×10^{-06}	1	2.185×10^{-06}	13.15	0.0023
W × L	9.265×10^{-06}	1	9.265×10^{-06}	55.73	< 0.0001
S × D	4.746×10^{-06}	1	4.746×10^{-06}	28.55	< 0.0001
S × L	2.869×10^{-06}	1	2.869×10^{-06}	17.26	0.0007
W^2	0.0000	1	0.0000	84.01	< 0.0001
S^2	3.796×10^{-06}	1	3.796×10^{-06}	22.83	0.0002
W^2L	7.135×10^{-06}	1	7.135×10^{-06}	42.92	< 0.0001
S^2D	1.470×10^{-06}	1	1.470×10^{-06}	8.85	0.0090
SD^2	2.951×10^{-06}	1	2.951×10^{-06}	17.75	0.0007
W^2S^2	0.0000	1	0.0000	83.43	< 0.0001
W^2D^2	0.0000	1	0.0000	72.78	< 0.0001
Residual	2.660×10^{-06}	16	1.662×10^{-07}		
Lack of fit	2.215×10^{-06}	10	2.215×10^{-07}	2.99	0.0964
Pure error	4.445×10^{-07}	6	7.409×10^{-08}		
Cor total	0.0001	30			

Notes: $R^2 = 0.9478$; adjusted $R^2 = 0.9021$; predicted $R^2 = 0.7969$.
Abbreviations: df: Degrees of freedom; MS: Mean square; SS: Sum of squares.

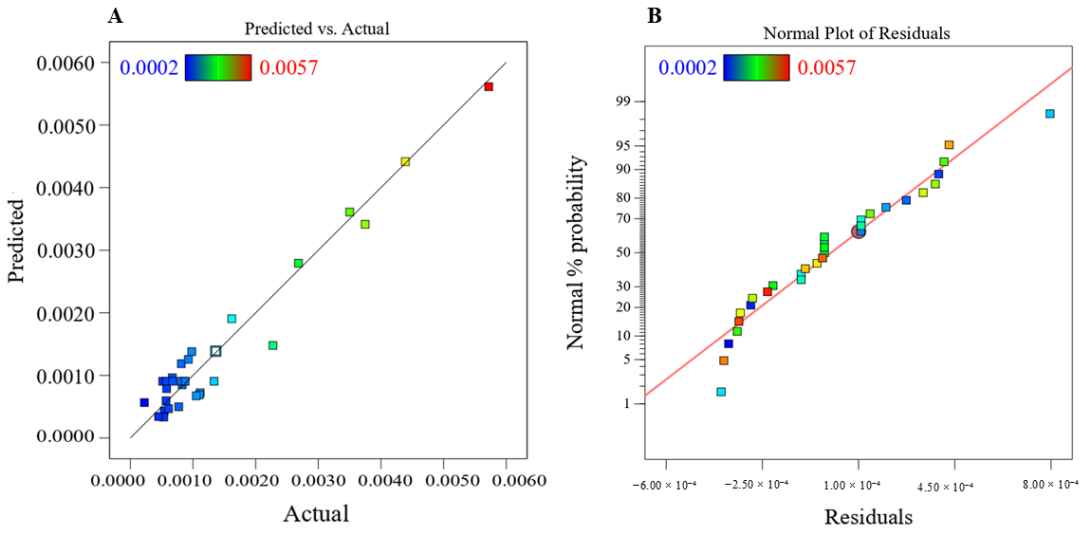

Figure 5. Specific wear rate. (A) Predicted vs. actual. (B) Residual plot.

The 3D surface plots in Figure 6A–6D illustrate the combined influence of different tribological parameters, including reinforcement, sliding speed, sliding distance, and applied load on the SWR. Figure 6A presents the combined effect of sliding speed and reinforcement on SWR. The plot shows that the SWR increases from 2.249 × 10^{-4} to 5.721 × 10^{-3} mm^3/N-mm, especially in the green-yellow region of the response surface. This indicates that the combined interaction of sliding speed and reinforcement substantially affects wear behavior. Figure 6B explores the interaction between sliding distance and sliding speed. The SWR changes from about 1.0 × 10^{-3} to 4.5 × 10^{-3} mm^3/N-mm, showing a gradual increase in wear rate across the surface. The curved shape of the plot confirms that sliding distance and sliding speed do not act independently but influence SWR together. Figure 6C shows the combined effect of sliding distance and reinforcement wt.% on SWR. The SWR rises from nearly 2.249 × 10^{-4} to 5.721 × 10^{-3} mm^3/N-mm, indicating that this interaction produces one of the highest wear responses among the plotted combinations. Figure 6D presents the effect of applied load and sliding speed on SWR. In this plot, the SWR varies from approximately 1.0 × 10^{-3} mm^3/N-mm to 4.0 × 10^{-3} mm^3/N-mm, and the inclined surface indicates a gradual increase in wear rate. The 3D surface plots confirm that SWR is significantly affected by the combined influence of reinforcement wt.%, sliding speed, sliding distance, and applied load, with the lowest value close to 2.249 × 10^{-4} mm^3/N-mm and the highest value reaching about 5.721 × 10^{-3} mm^3/N-mm.

3.2.2. Coefficient of friction

Table 5 presents the analysis of variance for the COF. The model is statistically significant (p = 0.0001), confirming it is suitable for predicting COF. Among the linear factors, sliding distance is the most influential (p = 0.0002), followed by reinforcement and sliding speed (p = 0.0012 and 0.0024, respectively). The interactions also strongly influence COF. The interaction between reinforcement and sliding speed (W × S) and sliding distance and applied load (D × L) are significant with p-values of 0.0145 and 0.0327, respectively. The quadratic term (S^2) and the interaction term (S^2D) were statistically significant (p = 0.0035 and p = 0.0032, respectively). The (WD^2) term was not statistically significant at the 5% level (p = 0.0587). The lack-of-fit test is not statistically significant (p = 0.9999), which is much greater than 0.05. This indicates no significant lack of fit and confirms that the developed model adequately represents the experimental data. The coefficient of determination (R^2) is 79.96%. The adjusted R^2 shows that 68.35% of the variation is explained after accounting for the number of model terms, while the predicted R^2 of 66.87% indicates acceptable predictive performance. The ANOVA results confirm that the developed model adequately predicts COF using **Equation 13**. Sliding distance is the most influential main factor, followed by reinforcement and sliding speed. The significant quadratic and higher-order terms further demonstrate that the COF behavior is nonlinear and depends on the combined influence of the process parameters.

$$\begin{aligned} COF = {} & 0.4537 - 0.0594W + 0.0448S - 0.0731D \\ & + 0.0077L + 0.0597WS + 0.0240WD \\ & + 0.0283SD - 0.0511DL - 0.0544S^2 \\ & + 0.0546WD^2 + 0.0916S^2D \end{aligned} \quad (13)$$

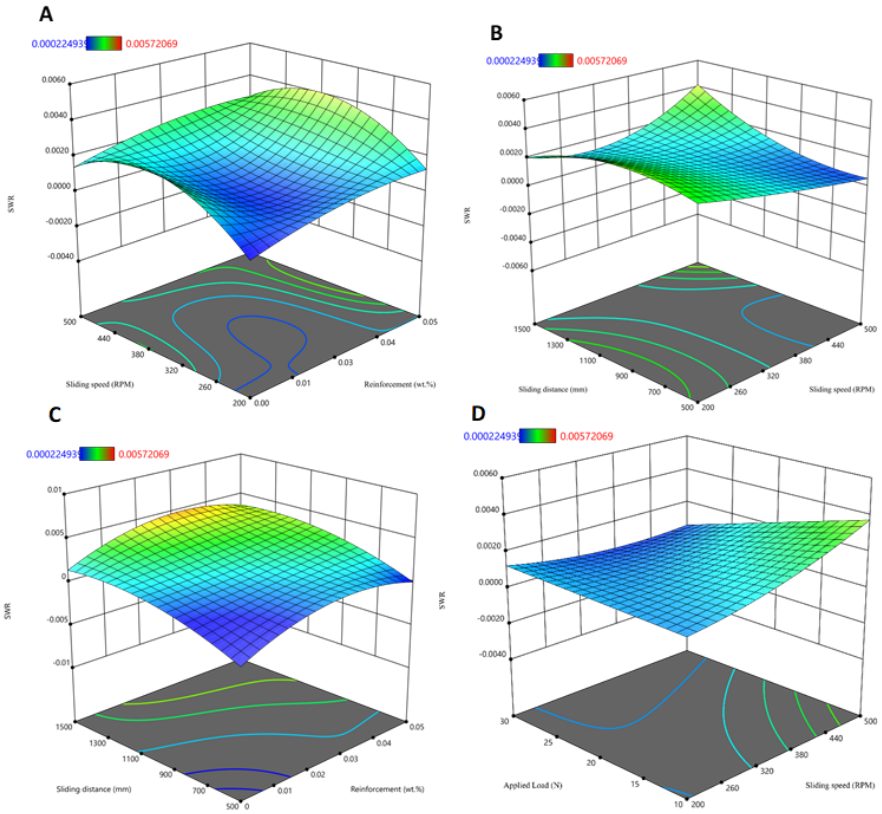

Figure 6. Three-dimensional surface plots of (A) speed vs. reinforcement, (B) sliding distance vs. speed, (C) sliding distance vs. reinforcement, and (D) applied load vs. speed for specific wear rates (SWRs).

Table 5. Analysis of variance for coefficient of friction

Source	SS	df	MS	*F*-value	*p*-value
Model	0.1491	11	0.0136	6.89	0.0001
Reinforcement (W)	0.0282	1	0.0282	14.35	0.0012
Speed (S)	0.0241	1	0.0241	12.22	0.0024
Sliding distance (D)	0.0427	1	0.0427	21.70	0.0002
Applied load (L)	0.0007	1	0.0007	0.3645	0.5532
WS	0.0142	1	0.0142	7.24	0.0145
WD	0.0023	1	0.0023	1.17	0.2936
SD	0.0032	1	0.0032	1.63	0.2168
DL	0.0104	1	0.0104	5.31	0.0327
S^2	0.0218	1	0.0218	11.07	0.0035
WD^2	0.0080	1	0.0080	4.04	0.0587
S^2D	0.0224	1	0.0224	11.36	0.0032
Residual	0.0374	19	0.0020	–	–
Lack of fit	0.0058	13	0.0004	0.0848	0.9999
Pure error	0.0316	6	0.0053	–	–
Cor total	0.1865	30	–	–	–

Notes: $R^2 = 0.7996$; adjusted $R^2 = 0.6835$; predicted $R^2 = 0.6687$.
Abbreviations: df: Degrees of freedom; MS: Mean square; SS: Sum of squares.

Figure 7A–7B illustrates and validates the accuracy and suitability of the predicted model for the COF. In Figure 7A, the relationship between the experimentally measured and predicted COF is shown. The COF values vary from 0.2403 to 0.5820. Most predicted values lie close to the inclined reference line, indicating good agreement between the experimental and predicted results. For example, the minimum experimental COF value of approximately 0.240 is predicted accurately at nearly 0.235–0.240. In the intermediate COF range of approximately 0.34–0.50, most predicted values remain close to their corresponding experimental values. However, a few deviations are observed at higher COF values. In particular, an experimental COF value of approximately 0.58 is predicted as nearly 0.46, while another experimental value of approximately 0.56 is predicted as nearly 0.59. Despite these deviations, the overall distribution of the data points around the reference line indicates acceptable predictive accuracy. Similarly, Figure 7B shows the normal probability distribution of the residuals. The residual values extend from −0.09 to +0.13, while most residuals are concentrated within the narrower range of approximately −0.04 to +0.04. Most points lie close to the straight reference line and cluster around zero residual, indicating that prediction errors are generally small and approximately normally distributed. Only a few observations at approximately −0.09, +0.05, and +0.13 deviate noticeably from the reference line. These limited deviations occur mainly at the extreme ends of the distribution and do not indicate a major systematic pattern. Therefore, the actual-versus-predicted and normal probability plots demonstrate that the developed model provides a satisfactory representation of the experimental COF data.

The 3D surface plots in Figure 8A–8D illustrate the influence of tribological parameters, including reinforcement, sliding speed, sliding distance, and applied load, on the COF. The color scale shows that the COF ranges from approximately 0.2403 to 0.582. Figure 8A presents the combined effect of sliding speed and reinforcement on COF. The plot shows a gradual reduction in COF from about 0.45–0.50 to nearly 0.25–0.30, indicating that the lower-friction region is obtained in the blue-green zone of the surface. Figure 8B shows the interaction between sliding distance and sliding speed, where the COF increases from approximately 0.30–0.35 to about 0.55–0.58. The yellow-red region in this plot represents the maximum COF, indicating a stronger interaction effect than in the other plots. Figure 8C presents the combined effect of sliding distance and reinforcement on COF. In this case, the COF varies moderately between about 0.35 and 0.50, and the smoother surface indicates a gradual change in frictional behavior. Figure 8D shows the effect of applied load and sliding distance on COF, with values approximately in the range of 0.40–0.55. The inclined surface confirms a noticeable combined influence of these parameters on friction. The plots confirm that the minimum COF is close to 0.2403, while the maximum COF reaches about 0.582. The curvature and gradient of the surfaces indicate that changes in sliding speed, sliding distance, reinforcement content, and applied load alter the frictional response, resulting in distinct low- and high-friction zones. These observations confirm that the developed response surface model adequately captures the interactive effects of the tribological parameters and predicts the composite's frictional behavior under different operating conditions.

3.3. Machine learning

Figure 9A–9B presents comparative parity plots of experimental and predicted values for tribological responses such as SWR and COF using three machine learning models. The blue, orange, and green data points represent MLR, RFR, and GBR, respectively. The black dashed diagonal line indicates the ideal prediction line, used to assess model accuracy. In Figure 9A, the SWR is approximately distributed from 0 to 0.0060. The MLR has the lowest prediction accuracy, with an R^2 of 0.539, showing that the data points scatter considerably around the parity line. Similarly, RFR and GBR improve prediction, with R^2 values of 0.830 and 0.975, as most points are closer to the ideal line, indicating excellent agreement between predicted and experimental wear-rate values. For the COF in Figure 9B, values range from 0.24 to 0.57. The R^2 values are 0.65, 0.723, and 0.824 for MLR, RFR, and GBR, respectively. The green points are closest to the ideal prediction line, confirming that gradient boosting has a strong predictive ability. GBR achieved the most accurate model for both SWR and COF, followed by RFR, while MLR shows the weakest performance. This trend suggests that nonlinear ensemble models capture complex material behavior more effectively than a simple linear approach. Figure 10A–10H compares the predictive performance of MLR, RFR, and GBR models for predicting SWR and COF using R^2, MSE, RMSE, relative RMSE (%), and MAE. For SWR prediction, Figure 10A reveals that the GBR model achieved the highest R^2 value of 0.975, followed by RFR with 0.83, while MLR showed the lowest value, 0.539. The error matrices further confirm the same trend, as shown in Figure 10C, Figure 10E, and Figure 10G, where the gradient boosting has a lower MSE, RMSE, and MAE values, 4.0783×10^{-08}, 0.0002, and 0.0002, respectively, followed by RFR with 0.00000028, 0.0005, and 0.0004, while the MLR model with large value of 0.00000076, 0.0009, and 0.0006. Therefore, for the SWR prediction, the gradient boosting model demonstrated the best overall accuracy.

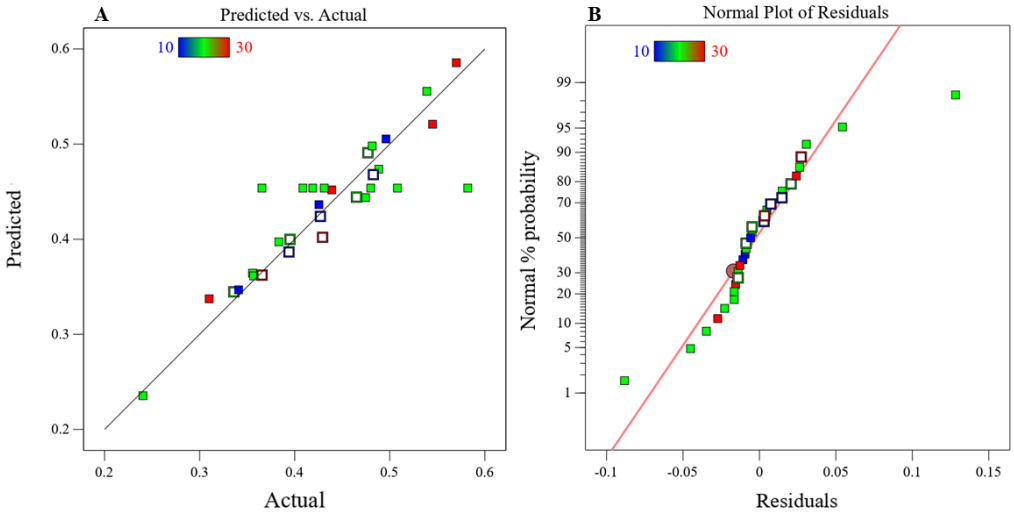

Figure 7. Coefficient of friction. (A) Prediction vs. actual. (B) Residual plot.

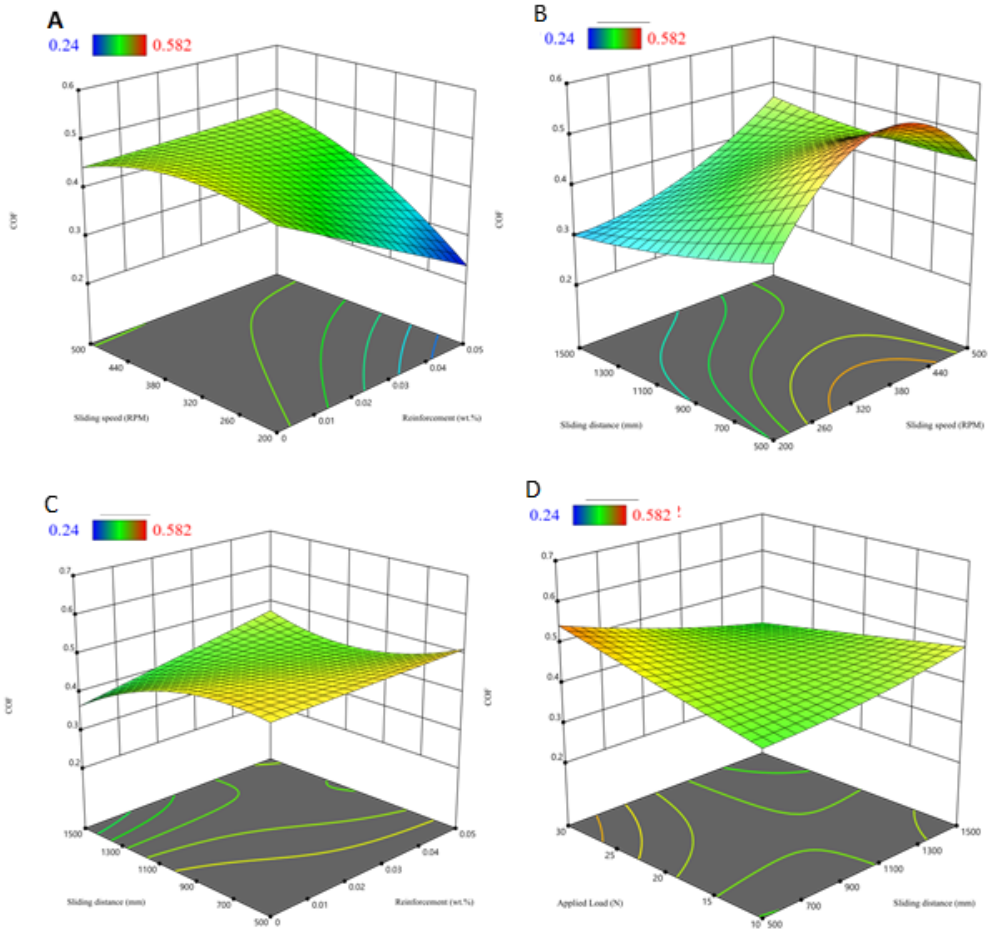

Figure 8. Three-dimensional surface plots of (a) speed vs. reinforcement, (b) sliding distance vs. speed, (c) sliding distance vs. reinforcement, and (d) applied load vs. sliding distance for coefficient of friction (COF).

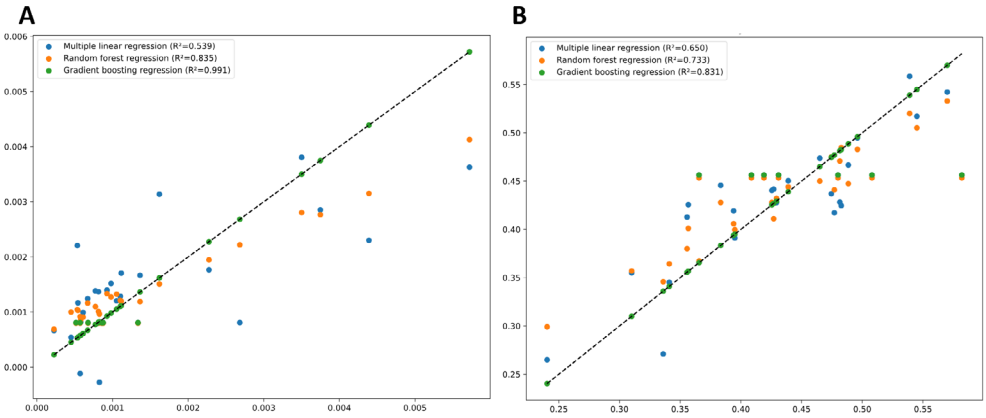

Figure 9. Comparative parity plots of machine learning for (A) specific wear rate and (B) coefficient of friction

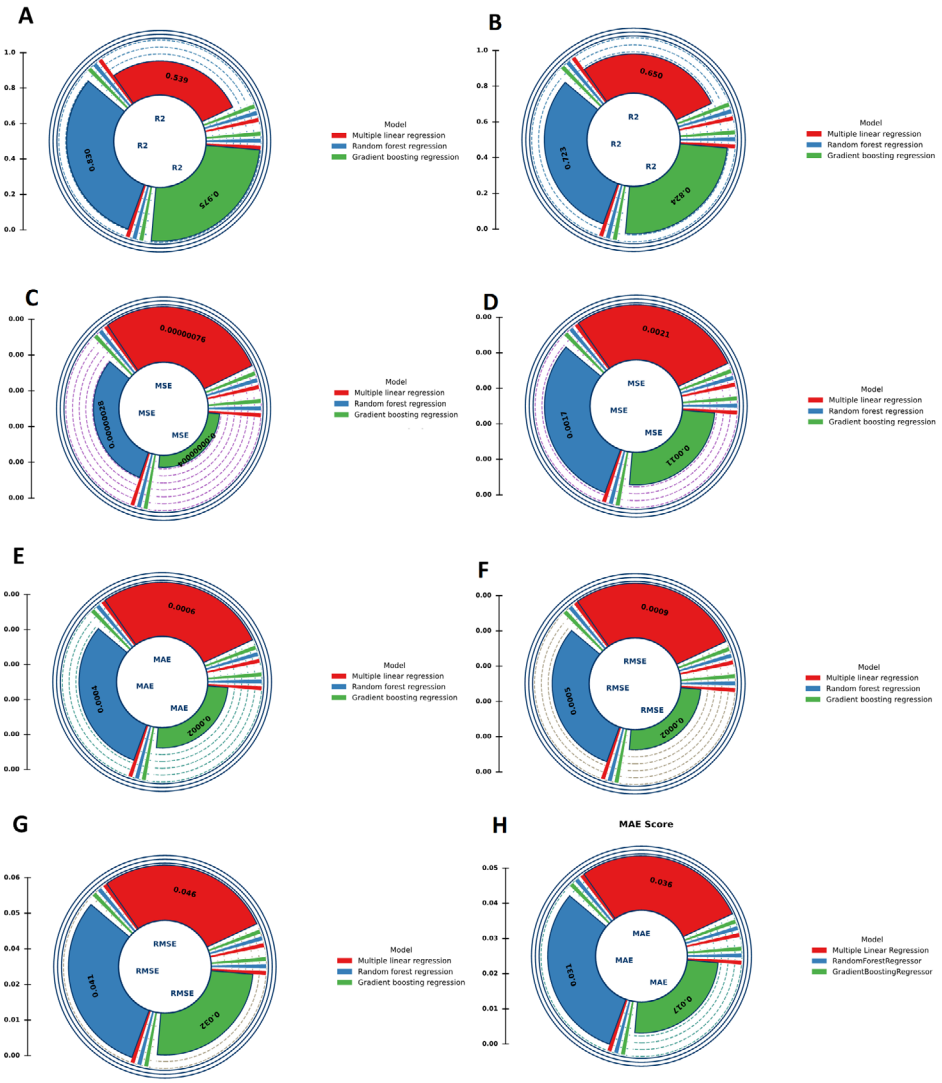

Figure 10. Comparison of predictive errors for multiple linear regression, random forest regression, and gradient boosting regression for SWR and COF. (A) R^2 score for SWR. (B) R^2 score for COF. (C) MSE for SWR. (D) MSE for COF. (E) RMSE for SWR. (F) RMSE for COF. (G) MAE for SWR. (H) MAE for COF. Abbreviations: COF: Coefficient of friction; MAE: Mean absolute error; MSE: Mean squared error; RMSE: Root mean squared error; SWR: Specific wear rate.

Similarly, for COF prediction, Figure 10B indicates that the GBR model again performed best, with an R^2 of 0.824, followed by RFR with 0.723, while MLR had the lowest value of 0.650. while the error matrices are revealed in the Figure 10D, Figure 10F, and Figure 10H show that the gradient boosting model achieved lowest MSE, RMSE, and MAE values of 0.0011, 0.032, and 0.017, respectively, whereas, RFR recorded 0.0017, 0.042, and 0.031, and MLR had the highest errors, of 0.0021, 0.046, and 0.036. These results indicate that the ensemble models captured the data pattern more effectively than the linear approach, with better predictive reliability. Therefore, the GBR model is considered for predicting the tribological performance of PLA composites reinforced with MXene because it consistently produced the lowest error across both figures and all metrics.

The confusion matrices in Figure 11 present the classification using MLR, RFR, and GBR for SWR. The evaluation is carried out using four classes, including Very Low, Low, High, and Very High. For the MLR model in Figure 11A, the classification performance is relatively weak, with correct predictions of 2 as Very Low, 3 as Low, 2 as High, and 7 as Very High; meanwhile, some significant misclassifications are observed, such as 4 Very Low being predicted as Low and High being misclassified as 2 Low and 3 Very High, respectively, indicating poor classification. In Figure 11B, the RFR model performance improves notably with a stronger diagonal pattern, correctly classifying 0 as Very Low, 3 as Low, 5 as High, and 7 as Very High, although 3 Very Low samples are mostly misclassified as Low and 5 as High, showing difficulty in distinguishing the lower classifications. Finally, the gradient boosting model in Figure 11C shows the best overall performance, with correct predictions of 2 as Very Low, 6 as Low, 5 as High, and 7 as Very High, and only minor misclassification such as 2 Low as High and 2 High as Low, 6 Very Low as Low, and 1 Very High misclassified as High, suggesting better categorical agreement within the evaluated dataset. However, the confusion matrices provide a supplementary assessment of categorical agreement and do not replace continuous regression metrics or independently demonstrate predictive performance on unseen data.

The confusion matrices in Figure 12 present the classification using machine learning models such as

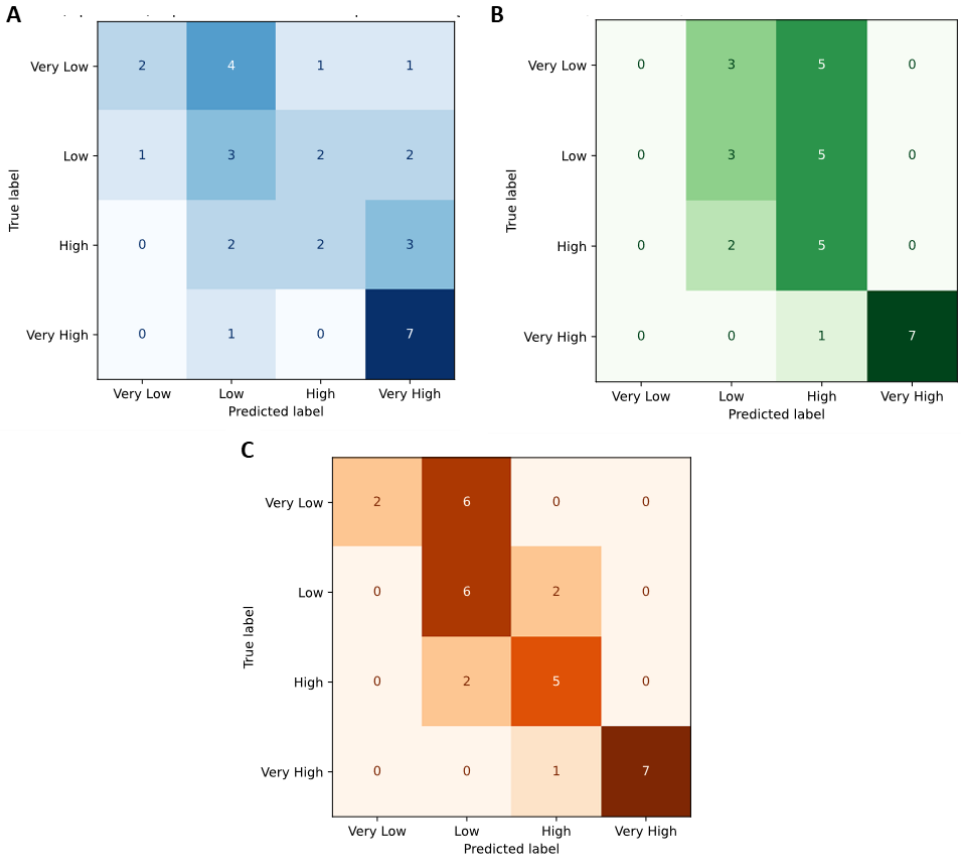

Figure 11. Confusion matrix of specific wear rate for (A) multiple linear regression, (B) random forest regression, and (C) gradient boosting regression

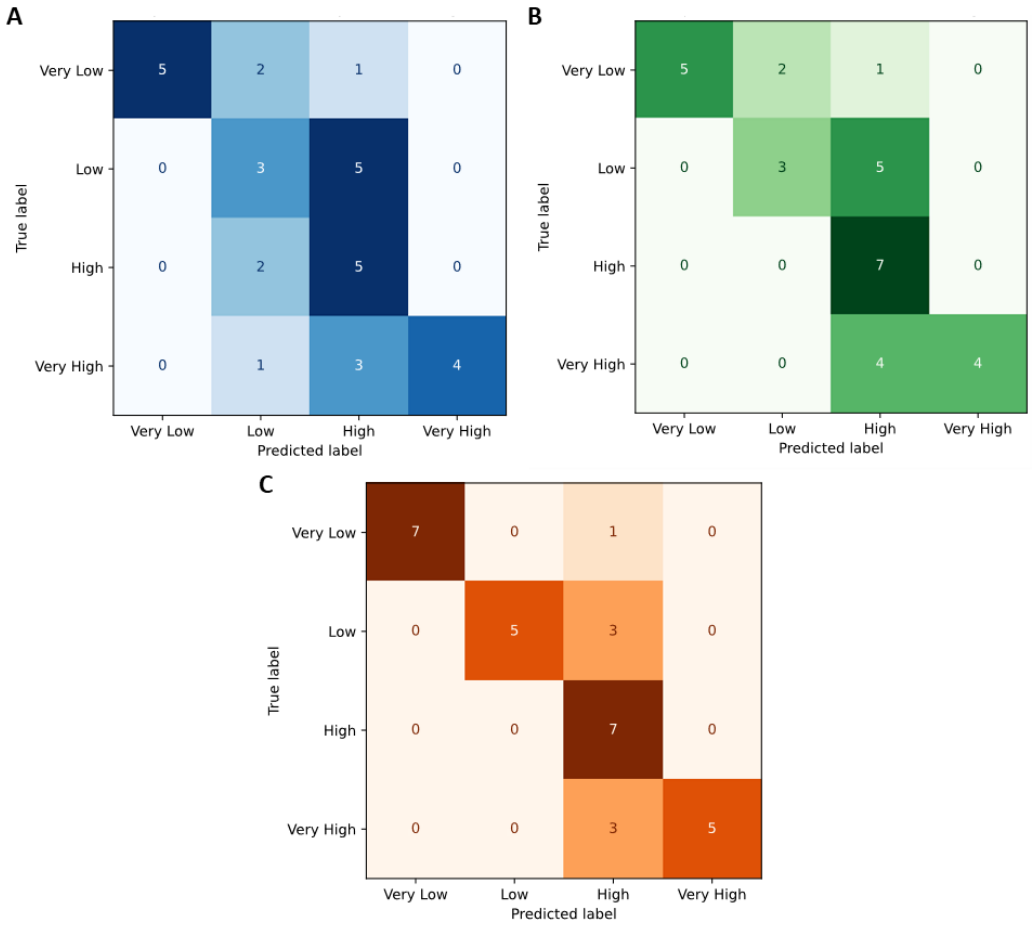

Figure 12. Confusion matrix of coefficient of friction for (A) multiple linear regression, (B) random forest regression, and (C) gradient boosting regression

MLR, RFR, and GBR for the COF. The performance was evaluated across four categories, including Very Low, Low, High, and Very High. For the MLR model in Figure 12A, the classifications are relatively limited, with only 5 correctly predicted as Very Low, 3 as Low, 5 as High, and 4 as Very High. Moreover, notable misclassifications occur, such as 2 Very Low predicted as Low, 2 High predicted as Low, 3 Very High predicted as High, and 1 Very High predicted as Low. Similarly, the RFR model in Figure 12B performs better with stronger diagonal dominance, correctly classifying 5 as Very Low, 3 as Low, 7as High, and 4 as Very High, although some errors persist, such as 2 Very Low misclassified as Low and 1 High predicted as Very Low, and 4 Very High partly misclassified as High. Finally, the gradient boosting model in Figure 12C shows the best performance, with correct predictions of 7 as Very Low, 5 as Low, 7 as High, and 5 as Very High, while misclassifications are minimal, including only 1 Very Low predicted as High, 3 Low predicted as High, and 3 Very High predicted as High, suggesting better categorical agreement than the other models within the evaluated dataset. However, these confusion matrices provide a supplementary assessment of categorical agreement and do not replace continuous regression metrics or independently demonstrate predictive performance on unseen data.

Figure 13 presents the SHAP-based feature importance analysis for SWR using MLR, RFR, and GBR models. For MLR (Figure 13A–13B), reinforcement content has the highest mean absolute SHAP value (approximately 0.00091), followed by sliding speed (0.00065), sliding distance (0.00034), and applied load, which contributes minimally. In contrast, the tree-based models assign the greatest contribution to applied load. For RFR (Figure 13C–13D), applied load has the highest mean absolute SHAP value (approximately 0.00013), followed by reinforcement content (0.000025), sliding distance (0.00001), and sliding speed (0.000008). Similarly, for GBR (Figure 13E–13F), applied load ranks highest (approximately 0.0009), followed by sliding distance (0.000015), reinforcement

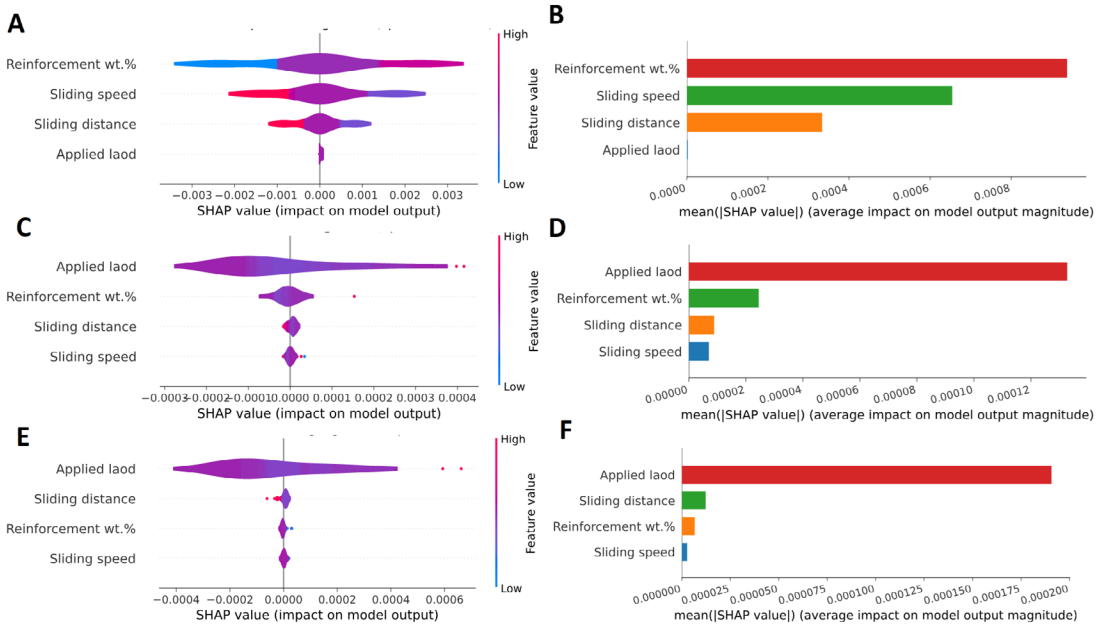

Figure 13. SHapley Additive exPlanations and feature values for specific wear rates. (A, B) Multiple linear regression. (C, D) Random forest regression. (E, F) Gradient boosting regression.

content (0.000008), and sliding speed (0.000004). These differences indicate that the models rely on the input features differently when generating predictions. SHAP values describe model-based feature contributions and should not be interpreted as direct physical effects or causal relationships.

Figure 14 presents SHAP-based feature importance for the COF, using violin and bar plots for MLR, RFR, and GBR models. For MLR (Figure 14A–14B), reinforcement content has the highest mean absolute SHAP value (0.09), followed by sliding speed (0.085), applied load (0.055), and sliding distance (0.01). In contrast, the tree-based models identify sliding speed as the feature with the greatest contribution to model predictions. For RFR (Figure 14C–14D), sliding speed shows SHAP values of approximately −0.04 to 0.02, followed by sliding distance and reinforcement content, while applied load has the lowest contribution. Similarly, for GBR (Figure 14E–14F), sliding speed has the largest SHAP-value spread (approximately −0.06 to 0.03), followed by sliding distance, reinforcement content, and applied load. These results indicate differences in how the models use the input features to generate predictions. However, SHAP values represent model-based feature contributions and do not independently establish physical mechanisms or causal relationships.

The correlation heatmap in Figure 15 presents that the factors such as reinforcement (wt.%), applied load, sliding distance, and sliding speed are independent, with near-zero correlations among the factors themselves like, reinforcement (wt.%) vs. applied load; reinforcement (wt.%) vs. sliding distance; reinforcement wt.% vs. sliding speed; applied load vs. sliding distance; applied load vs. sliding speed; and sliding distance vs. sliding speed; Regarding the responses, SWR shows that the reinforcement (wt.%) and applied loads have negative correlation of −0.05, and −0.01 respectively, while sliding distance and sliding speed have positive correlation with 0.10 and 0.06. In contrast, COF shows the strongest associations, with positive correlations with sliding speed and applied load (0.36 and 0.06) and negative correlations with sliding distance (−0.34) and reinforcement (wt.%) (−0.33). These values indicate that COF is more sensitive to sliding speed, sliding distance, and reinforcement content, whereas SWR is not strongly governed by any single parameter linearly, suggesting that the tribological response is likely controlled by combined or nonlinear effects rather than simple one-to-one relationships.

4. Experimental validation

Table 6 presents the experimental validation results of the machine learning models using R^2, MSE, RMSE, MAE, and MAPE. Compared with the training results, the SWR (R^2) value for MLR decreased from 0.5390 to 0.0708 during experimental validation, whereas RFR decreased from 0.8300 to 0.7464 and GBR decreased from 0.9750 to

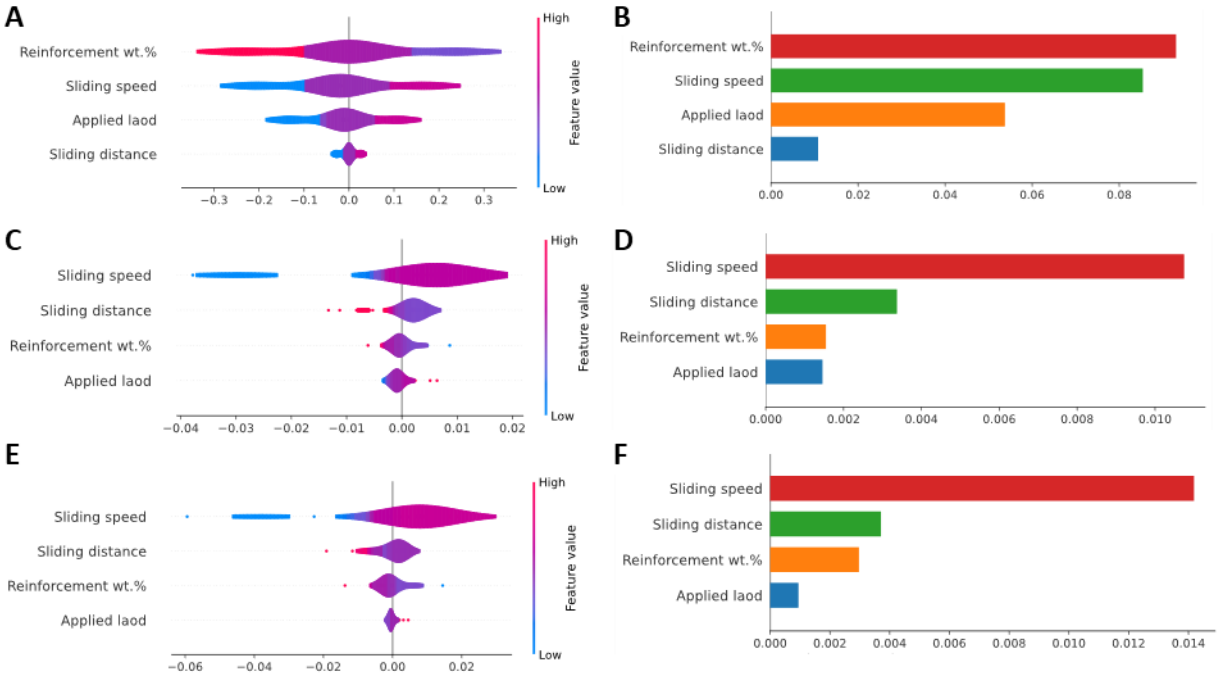

Figure 14. SHapley Additive exPlanations and feature values for coefficients of friction. (A, B) Multiple linear regression. (C, D) Random forest regression. (E, F) Gradient boosting regression.

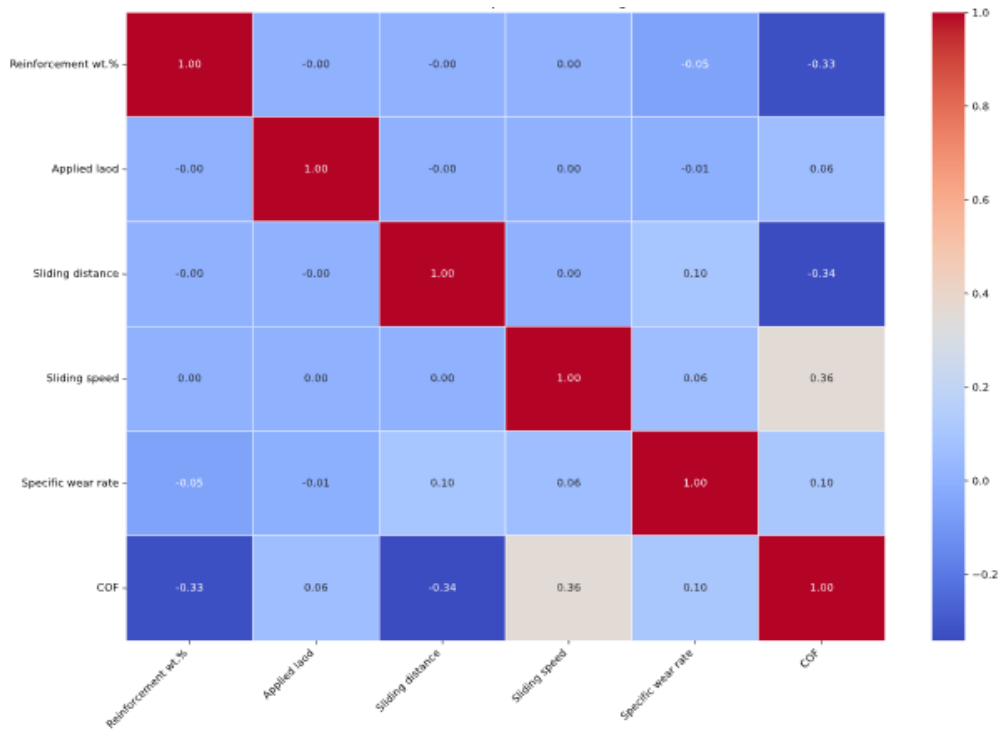

Figure 15. Correlation heat map for factors and response

Table 6. Performance of machine learning models during experimental validation

Model	Responses	R^2	MSE	RMSE	MAE	MAPE
MLR	SWR (mm^3/N-mm)	0.0708	1.79E-06	0.00133	0.00089	40.873
	COF	0.6500	0.0014	0.0378	0.03141	6.797
RFR	SWR (mm^3/N-mm)	0.7464	4.89E-07	0.00069	0.00048	22.481
	COF	0.6312	0.0015	0.0389	0.02927	5.940
GBR	SWR (mm^3/N-mm)	0.8879	2.16E-07	0.00046	0.00037	18.314
	COF	0.771	0.00018	0.0136	0.01296	2.9793

Abbreviations: COF: Coefficient of friction; GBR: Gradient boosting regression; MAE: Mean absolute error; MAPE: Mean absolute percentage error; MLR: Multiple linear regression; MSE: Mean squared error; RFR: Random forest regression; RMSE: Root mean squared error; SWR: Specific wear rate.

0.8879. For COF, the R^2 decreased from 0.650 to 0.631 for RFR (2.92%), while MLR remained unchanged at 0.650 and GBR decreased from 0.824 to 0.771 (6.43%). Among the three models, GBR maintained the highest R^2 during experimental validation for both SWR (0.8879) and COF (0.771). The results indicate that GBR provided the strongest overall predictive performance.

5. Conclusion

This current research focused on the tribological performance of FDM-fabricated PLA–MXene ($Ti_3C_2T_x$) nanocomposites, which were analyzed using experiments, RSM, and machine learning models to understand and predict wear and friction behavior. The main conclusions are summarized:

- The tribological responses showed significant variation, with SWR ranging from 2.2×10^{-4} to 5.7×10^{-3} mm^3/Nmm and COF from 0.240 to 0.582.
- ANOVA revealed that applied load was the most influential factor for SWR, while sliding distance, reinforcement content, and sliding speed significantly affected COF.
- The developed RSM models demonstrated good predictive capability with R^2 values of 94.78% for SWR and 79.96% for COF, confirming the adequacy of the statistical models.
- During experimental validation, GBR achieved R^2 values of 0.8879 for SWR and 0.771 for COF, compared with training values of 0.975 and 0.824, respectively. This corresponds to a deviation of less than 10% for both SWR and COF.
- SHAP analysis identified the relative contributions of applied load, reinforcement content, sliding distance, and sliding speed to the model predictions, with their importance varying according to the response and the machine-learning model.

Future research should explore advanced modeling and optimization methodologies, supported by a larger experimental dataset and additional mechanical tests to improve prediction accuracy and reliability. Real-time defect monitoring, adaptive process control, filament size prediction, and the effects of deposition geometry and processing conditions on FDM-printed PLA/MXene composites will also be investigated.[41,42]

Acknowledgement

The authors extend their acknowledgment to the financial support of the European Union under the REFRESH-Research Excellence for Region Sustainability and High-tech Industries project number CZ.10.03.01/00/22_003/0000048 via the Operational Programme Just Transition.

Funding

None.

Conflict of interest

The authors declare that they have no competing interests.

Author contributions

Conceptualization: Sundarasetty Harishbabu, Santosh Kumar Sahu
Formal analysis: All authors
Investigation: Sundarasetty Harishbabu, Santosh Kumar Sahu, Jana Petrů
Writing–original draft: Sundarasetty Harishbabu
Writing–review and editing: Santosh Kumar Sahu, P. S. Rama Sreekanth, Ravi Kumar V, Jana Petrů

Ethics approval and consent to participate

Not applicable.

Consent for publication

Not applicable.

Availability of data

Data are available from the corresponding author upon reasonable request.

Further disclosure

ChatGPT (GPT-6, OpenAI, USA) was used solely to improve the language, grammar, readability, and clarity of the manuscript. No AI tools were used to generate scientific insights, analyze or interpret data, or draw scientific conclusions. The authors reviewed and approved all AI-assisted language revisions and take full responsibility for the content of the manuscript.

References

1. Sheikh T, Behdinan K. Fused deposition modelling of thermoplastic polymer nanocomposites: a critical review. *C*. 2024;10(2):29.

   doi: 10.3390/c10020029

2. Ahmed R, Dola IS, Ahmed S, Rahman MM, Shanto TA, Taylor R. A review of design and fabrication strategies for thermoplastic lightweight thin-walled stiffened shells and lattice structures utilizing fused-filament fabrication (FFF). *Int J Adv Manuf Technol*. 2026;144(9-10):6111-6158.

   doi: 10.1007/s00170-026-18078-6

3. Leśniowski J, Stawiarski A, Barski M. Enhancing the performance of FFF-printed parts: a review of reinforcement and modification strategies for thermoplastic polymers. *Materials*. 2025;18(22):5185.

   doi: 10.3390/ma18225185

4. Zotti A, Paduano T, Napolitano F, Zuppolini S, Zarrelli M, Borriello A. Fused deposition modeling of polymer composites: development, properties and applications. *Polymers*. 2025;17(8):1054.

   doi: 10.3390/polym17081054

5. Plamadiala I, Croitoru C, Pop MA, Roata IC. Enhancing polylactic acid (PLA) performance: a review of additives in fused deposition modelling (FDM) filaments. *Polymers*. 2025;17(2):191.

   doi: 10.3390/polym17020191

6. Trivedi AK, Gupta MK. A comprehensive review on 3D printing of polymer based composites through FDM: materials, processing parameters, challenges and future scope. *Proc Inst Mech Eng L J Mater Des Appl*. 2025;240(7):1051-1075.

   doi: 10.1177/14644207251360284

7. Kumar V, Bharat N, Mishra V. Mechanical and tribological enhancement of graphene-reinforced PLA composites for sustainable applications. *J Inorg Organomet Polym Mater*. 2026;36:1435-1451.

   doi: 10.1007/s10904-025-03783-8

8. Al Abir A, Chakrabarti D, Trindade B. Fused filament fabricated poly(lactic acid) parts reinforced with short carbon fiber and graphene nanoparticles with improved tribological properties. *Polymers*. 2023;15(11):2451.

   doi: 10.3390/polym15112451

9. Ramachandran MG, Rajeswari N. Influence of nano silica on mechanical and tribological properties of additive manufactured PLA bio nanocomposite. *Silicon*. 2022;14(2):703-709.

   doi: 10.1007/s12633-020-00878-4

10. Vishal K, Rajkumar K, Sabarinathan P, Dhinakaran V. Mechanical and wear characteristics investigation on 3D printed silicon filled poly(lactic acid) biopolymer composite fabricated by fused deposition modeling. *Silicon*. 2022;14(15):9379-9391.

    doi: 10.1007/s12633-022-01712-9

11. Sirin S, Yıldırım Çağrı Vakkas, Sevinç AM, Ceylan A, Kara Mİ. Evaluation of wear and friction properties of graphite modified Lubri polylactic acid with various infill fabricated by additive manufacturing techniques. *Polym Compos*. 2024;45(17):16133-16152.

    doi: 10.1002/pc.28895

12. Batista M, Del Sol I, Gómez-Parra Á, Vazquez-Martinez JM. Tribological performance of additive manufactured PLA-based parts. *Polymers*. 2024;16(17):2529.

    doi: 10.3390/polym16172529

13. Zawadzki P, Rybarczyk J, Patalas A, *et al.* Tribological properties of fused deposition modeling-printed polylactic acid and PLA-CF: extrusion temperature and internal structure. *J Tribol*. 2026;148(2):024202.

    doi: 10.1115/1.4068991

14. Fouly A, Assaifan AK, Alnaser IA, Hussein OA, Abdo HS. Evaluating the mechanical and tribological properties of 3D printed polylactic-acid (PLA) green-composite for artificial implant: hip joint case study. *Polymers*. 2022;14(23):5299.

    doi: 10.3390/polym14235299

15. Singh S, Attri RK, Trivedi S. Optimization of FDM 3D printing process parameters for improving wear characteristics of PLA-nGr composite using Taguchi DOE. *J Mater Eng Perform*. 2025;34(14):15179-15187.

    doi: 10.1007/s11665-024-10170-w

16. Hozdić E, Hozdić E. Mechanical parameters and microstructural evolution of FDM-printed PLA and PLA+CF under variable infill architecture and lubricant exposure. *Polymers*. 2026;18(1):72.

doi: 10.3390/polym18010072

17. Mzali S, Elwasli F, Mezlini S, Hajlaoui K, Ksir H. Experimental investigation of tribological behavior of FDM-PLA surfaces. *Proc Inst Mech Eng L J Mater Des Appl*. 2025;239(4):760-775.

doi: 10.1177/14644207241312974

18. Lasch G, Sostizzo GG, Gehlen GS, *et al.* Exploring the tribological properties of 3D printed polymer composites: an experimental study. *Polym Compos*. 2025;47(8):6840-6858.

doi: 10.1002/pc.70591

19. Keshavamurthy R, Tambrallimath V, Patil S, Rajhi A, Duhduh A, Khan T. Mechanical and wear studies of boron nitride-reinforced polymer composites developed via 3D printing technology. *Polymers*. 2023;15(22):4368.

doi: 10.3390/polym15224368

20. Abdulla M, Onkar PS, Haragopal VV, Akhil S, Bagal DK, Sharma RM. ANN-based dry sliding wear behavior prediction for test samples made of 3D printed PLA. *Mater Today Proc*. Published online 2024.

doi: 10.1016/j.matpr.2024.03.012

21. Ahmad H, Ahmed A, Waheed S, *et al.* Advancements in fused deposition modelling (FDM): a comparison of advanced composite materials, optimization strategies, and AI/ML integration. *Adv Mater Process Technol*. 2026;12(2):312-350.

doi: 10.1080/2374068X.2026.2630731

22. Subba CB, Rai DP, Tursunov ME, Dekhkonov AT, Pachuau Z. Comprehensive review of MAX phase and MXene materials: synthesis, properties, and applications. *Carbon Lett*. 2025;35(6):2485-2570.

doi: 10.1007/s42823-025-00979-3

23. Ma T, Zhang Y, Ruan K, *et al.* Advances in 3D printing for polymer composites: a review. *InfoMat*. 2024;6(6).

doi: 10.1002/inf2.12568

24. Harishbabu S, Alrasheedi NH, Louhichi B, Sreekanth PSR, Sahu SK. Machine learning-assisted synergistic optimization of 3D printing parameters for enhanced mechanical properties of PLA/boron nitride nanocomposites. *Machines*. 2025;13(10):949.

doi: 10.3390/machines13100949

25. Uddin MS, Sidek MFR, Faizal MA, Ghomashchi R, Pramanik A. Evaluating mechanical properties and failure mechanisms of fused deposition modeling acrylonitrile butadiene styrene parts. *J Manuf Sci Eng*. 2017;139(8):081018.

doi: 10.1115/1.4036713

26. Salguero J, Iglesias P, Vazquez-Martinez JM, Batista M, Del Sol I. A comparative study of disk wear volume evaluation of Al2024 based on ASTM G99. *ASME Int Mech Eng Congr Expo*. 2022;9.

doi: 10.1115/IMECE2022-94625

27. Sundarasetty H, Sahu SK. Tribological behavior of PLA reinforced with boron nitride nanoparticles using Taguchi and machine learning approaches. *Results Eng*. 2025;26:104772.

doi: 10.1016/j.rineng.2025.104772

28. Ferreira SC, Bruns RE, Ferreira HS, *et al.* Box-Behnken design: an alternative for the optimization of analytical methods. *Anal Chim Acta*. 2007;597(2):179-186.

doi: 10.1016/j.aca.2007.07.011

29. Harishbabu S, Salhi A, Jamel L, *et al.* Machine learning and response surface methodology for optimization and prediction of tribological performance of PLA/rice husk biochar composites. *Sci Rep*. 2026;16(1):20938.

doi: 10.1038/s41598-026-51463-5

30. Harishbabu S, Alrasheedi NH, Louhichi B, Sahu SK, Ma Q. Optimization and prediction of mechanical properties of additively manufactured PLA/GNP composites via response surface methodology and machine learning models. *Polymers*. 2025;17(21):2894.

doi: 10.3390/polym17212894

31. Kohan-Baghkheirati E, Ahmadi-Bootegaz S, Zaferanieh M, Sanei M. Hybrid response surface methodology-support vector machine modeling approach enhanced the efficiency of optimization for sansevieria propagation. *Plant Cell Tissue Organ Cult*. 2026;164(1):10.

doi: 10.1007/s11240-025-03323-9

32. Mohammed AJ, Mohammed AS, Mohammed AS. Prediction of tribological properties of UHMWPE/SiC polymer composites using machine learning techniques. *Polymers*. 2023;15(20):4057.

doi: 10.3390/polym15204057

33. Naidu M, Bhosale A, Munde Y, Salunkhe S, Hussein HMA. Wear and friction analysis of brake pad material using natural hemp fibers. *Polymers*. 2022;15(1):188.

doi: 10.3390/polym15010188

34. Chicco D, Warrens MJ, Jurman G. The coefficient of determination R-squared is more informative than SMAPE, MAE, MAPE, MSE and RMSE in regression analysis evaluation. *PeerJ Comput Sci*. 2021;7:e623.

doi: 10.7717/peerj-cs.623

35. Karadag A, Ulkir O. Multi-parameter optimization, machine learning-based prediction, and surface characterization of bio-based FDM composites. *J Appl Polym Sci*. 2026;143(33).

doi: 10.1002/app.70953

36. Palabıyık S, Akkan T. Evaluation of water quality based on artificial intelligence: performance of multilayer perceptron neural networks and multiple linear regression versus water

quality indexes. *Environ Dev Sustain*. 2024;28(2):2717-2740.

doi: 10.1007/s10668-024-05075-6

37. Wang C, Zhang Q, Tao M, *et al.* Estimation of seasonal ecological water demand in arid zone of Northwest China: an approach using the LSTM-random forest regression model. *J Environ Manage*. 2026;397:128240.

doi: 10.1016/j.jenvman.2025.128240

38. Hu X, Liu S, Liu Y. Using gradient boosting regression trees to identify cost drivers of laparoscopic surgery in elderly patients. *Discov Artif Intell*. 2025;6(1):14.

doi: 10.1007/s44163-025-00702-1

39. Kumar GSP, Keshavamurthy R, Thomas S, *et al.* Tribological characteristics of CNT/graphene reinforced PLA-based polymer composites fabricated via FDM process. *J Bio Tribo Corros*. 2026;12(4):156.

doi: 10.1007/s40735-026-01210-0

40. Wang Y, Lim S, Luo JL, Xu ZH. Tribological and corrosion behaviors of Al2O3/polymer nanocomposite coatings. *Wear*. 2006;260(9-10):976-983.

doi: 10.1016/j.wear.2005.06.013

41. Yao Y, Gao Q, Yu K, *et al.* Study on the formation mechanism of viscoplastic line deposition for predicting filament width. *Mater Des*. 2025;249:113550.

doi: 10.1016/j.matdes.2024.113550

42. Yu K, Yao Y, Zhang W, *et al.* Defects, monitoring, and AI-enabled control in soft material additive manufacturing: a review. *Virtual Phys Prototyp*. 2025;20(1).

doi: 10.1080/17452759.2025.2588456